Astronomy & Astrophysics manuscript no. output
April 7, 2026

EPRV Asteroseismology of the K dwarfs GJ 570 A and GJ 783 A with ESPRESSO

Empirical mode-amplitude scaling in tension with 3D convection simulations

T. L. Campante[1,2], Y. Zhou[3], Y. Li[4], H. Kjeldsen[5], R. R. Costa[1,2], A. W. Neitzel[1,2], J. H. C. Martins[1], A. M. Silva[1,2], V. Adibekyan[1,2], J. Gomes da Silva[1], J. R. Larsen[5], S. G. Sousa[1,2], T. R. Bedding[6], D. Bossini[7], W. J. Chaplin[8], E. Corsaro[9], M. S. Cunha[1], M. Deal[10], D. Huber[4], M. N. Lund[5], M. S. Lundkvist[5], T. S. Metcalfe[11], M. J. P. F. G. Monteiro[1,2], and N. C. Santos[1,2]

[1] Instituto de Astrofísica e Ciências do Espaço, Universidade do Porto, Rua das Estrelas, 4150-762 Porto, Portugal
e-mail: tiago.campante@astro.up.pt
[2] Departamento de Física e Astronomia, Faculdade de Ciências da Universidade do Porto, Rua do Campo Alegre, s/n, 4169-007 Porto, Portugal
[3] Rosseland Centre for Solar Physics (RoCS), Institute of Theoretical Astrophysics, University of Oslo, PO Box 1029, Blindern, 0315 Oslo, Norway
[4] Institute for Astronomy, University of Hawai'i, 2680 Woodlawn Drive, Honolulu, HI 96822, USA
[5] Stellar Astrophysics Centre (SAC), Department of Physics and Astronomy, Aarhus University, Ny Munkegade 120, 8000 Aarhus C, Denmark
[6] Sydney Institute for Astronomy (SIfA), School of Physics, University of Sydney, NSW 2006, Australia
[7] INAF – Osservatorio Astronomico di Padova, Vicolo dell'Osservatorio 5, 35122 Padova, Italy
[8] School of Physics and Astronomy, University of Birmingham, Edgbaston, Birmingham B15 2TT, UK
[9] INAF – Osservatorio Astrofisico di Catania, Via S. Sofia 78, 95123 Catania, Italy
[10] LUPM, Université de Montpellier, CNRS, Place Eugène Bataillon, 34095 Montpellier, France
[11] Center for Solar-Stellar Connections, WDRC, 9020 Brumm Trail, Golden, CO 80403, USA

Received Month Day, 2026

ABSTRACT

Context. Solar-like oscillations in K dwarfs have intrinsically low amplitudes, making them challenging to detect in space-based photometry. The advent of Extremely Precise Radial Velocity (EPRV) instrumentation enables Doppler asteroseismology in the mid-K regime, providing a new opportunity to test mode-excitation and damping physics.
Aims. We investigate the scaling of oscillation amplitudes with stellar parameters and assess whether 3D surface convection simulations reproduce the observed amplitude behavior.
Methods. High-cadence ESPRESSO radial-velocity time series were obtained over five and six consecutive nights for the K dwarfs GJ 570 A (K4 V) and GJ 783 A (K2.5 V), respectively. We identified oscillation modes from weighted power spectra and extracted them via sine-wave fitting following spectral deconvolution. Peak mode amplitudes were measured from heavily smoothed power spectra. For comparison, we performed 3D radiative-hydrodynamical simulations including excitation and damping-rate calculations.
Results. We measured 6 modes for GJ 570 A and 24 for GJ 783 A ($\ell = 0$–2, and $\ell = 3$ for GJ 783 A). The peak radial-mode amplitudes are $2.57 \pm 0.52\,\mathrm{cm\,s^{-1}}$ and $4.90 \pm 0.81\,\mathrm{cm\,s^{-1}}$, respectively. Combined with previous Doppler detections, these results support a transition from an $\sim (L/M)^{0.7}$ amplitude scaling to a steeper $\sim (L/M)^{1.5}$ scaling, occurring near the G/K-dwarf boundary toward decreasing L/M. In contrast, 3D simulations predict an $\sim (L/M)^{0.9}$ scaling for K dwarfs, revealing tension between observations and first-principles convection models.
Conclusions. EPRV asteroseismology extends into the mid-K regime and exposes a steep mode-amplitude scaling that our 3D convection simulations do not reproduce. This discrepancy points to missing physics in our implementation of convection–pulsation coupling and/or limitations in the adopted modeling assumptions, motivating further theoretical investigation.

Key words. Asteroseismology – Stars: individual: GJ 570 A, GJ 783 A – Stars: late-type – Stars: oscillations (including pulsations) – Techniques: radial velocities

1. Introduction

Notable progress in asteroseismology has been made due to missions such as Convection, Rotation and planetary Transits (CoRoT; Baglin et al. 2006), *Kepler*/K2 (Borucki et al. 2010; Howell et al. 2014), and the Transiting Exoplanet Survey Satellite (TESS; Ricker et al. 2015). These missions have delivered high-precision photometric data from space, allowing for in-depth investigations of the internal structures of solar-type and red-giant stars, which exhibit solar-like oscillations driven by convection (Chaplin & Miglio 2013; Aerts 2021). Despite this, the small-amplitude solar-like oscillations in K dwarfs (amplitudes below a few parts per million or, equivalently, 10 $\mathrm{cm\,s^{-1}}$; Kjeldsen et al. 2008a; Verner et al. 2011) remain extremely challenging to detect in space-based photometry (Mathur et al. 2017;

Hatt et al. 2023). This difficulty persists even with access to multi-year *Kepler* (e.g., Campante et al. 2015; Lundkvist et al. 2016) and multi-sector TESS (e.g., Campante et al. 2016; Hon et al. 2024; Lund et al. 2025) observations. As a result, only a handful of dwarfs cooler than the Sun show oscillations in photometry, with detections dropping off sharply below ∼5500 K (see Fig. 1).

Doppler velocity observations offer a viable alternative to space-based photometry. Stellar "noise" from activity and granulation is significantly lower in Doppler than in photometry (Harvey 1988; Grundahl et al. 2007), resulting in a higher signal-to-noise ratio (S/N) over the typical oscillation timescales (Hon et al. 2024; Kjeldsen et al. 2025). This motivated several pre-*Kepler* radial-velocity (RV) campaigns targeting late-G/early-K dwarfs (e.g., Kjeldsen et al. 2005; Carrier & Eggenberger 2006; Teixeira et al. 2009), using then state-of-the-art spectrographs such as the High Accuracy Radial velocity Planet Searcher (HARPS; Mayor et al. 2003) and the Ultraviolet and Visual Echelle Spectrograph (UVES; Dekker et al. 2000). These pioneering efforts helped establish a lower effective temperature ($T_{\rm eff}$) bound for cool-dwarf asteroseismology (see Fig. 1). However, limited RV precision and/or relatively small apertures restricted detections to only the very brightest dwarfs.

Advances in Doppler precision, driven by the search for Earth-like planets, are providing a renewed opportunity for detecting low-amplitude oscillations, with Extremely Precise Radial Velocity (EPRV) techniques currently achieving 20–30 cm s^{-1} precision in a single exposure (for a recent review, see Burt et al. 2025). The few-minute oscillation periods typical of K dwarfs demand a fast observational cadence, requiring exposures as short as ∼25 s (with the remaining cadence budget allocated to readout). Achieving the necessary RV precision within such short integrations calls for an optimal combination of instrumental stability and large collecting area. The last couple of years have witnessed a groundbreaking resurgence of observational campaigns targeting K dwarfs (see Fig. 1), fueled by EPRV instruments mounted on large-aperture telescopes, namely, the Echelle SPectrograph for Rocky Exoplanets and Stable Spectroscopic Observations (ESPRESSO; Pepe et al. 2021) on the Very Large Telescope (VLT) and the Keck Planet Finder (KPF; Gibson et al. 2024) on the Keck I telescope. ESPRESSO and KPF are among the very few instrumental setups capable of achieving this level of performance, with a coordinated all-sky effort to characterize cool seismic dwarfs currently underway, leveraging both facilities.

A 6-night pilot campaign conducted with ESPRESSO on the fourth-magnitude K5 dwarf ϵ Indi (Campante et al. 2024) demonstrated the potential of EPRVs for cool-dwarf asteroseismology, enabling detection of solar-like oscillations with a peak amplitude of 2.6 cm s^{-1} (or a mere ∼14% of the solar value; see also Lundkvist et al. 2024). This followed an earlier claim of p-mode detection in the nearly ten times fainter K3 dwarf HD 40307 (Pepe et al. 2021), a result that was subsequently ruled out (Campante et al. 2024). Hon et al. (2024) later detected oscillations in the K0 V star σ Draconis using only a single night of observations with KPF. While 20-second cadence TESS photometry from 14 sectors also showed oscillations for this star, the KPF data revealed oscillation modes over a considerably broader frequency range due to their higher S/N. More recently, based on four nights of data collected with KPF, Li et al. (2025a) detected oscillations in the K3 V star HD 219134, extracting 25 mode frequencies with angular degree $\ell = 0$–3, and determined its benchmark mass, radius, and age via asteroseismology.

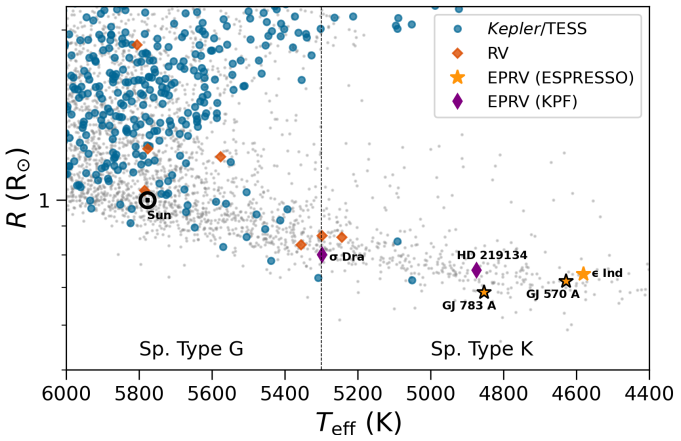

Fig. 1: Stellar radius–effective temperature diagram highlighting asteroseismic detections from *Kepler* and TESS photometry (blue circles; Mathur et al. 2017; Hatt et al. 2023; Lund et al. 2025), earlier RV campaigns (red diamonds; see Arentoft et al. 2008; Kjeldsen et al. 2008a, and references therein), and recent EPRV observations of K dwarfs with ESPRESSO (orange star symbols; Campante et al. 2024) and KPF (purple thin diamonds; Hon et al. 2024; Li et al. 2025a). The two stars analyzed in this work, GJ 570 A and GJ 783 A, are highlighted among the ESPRESSO sample. The stellar background sample (gray dots) is taken from the TESS Input Catalog (TIC; Stassun et al. 2019). The Sun is denoted by its usual symbol. Spectral types G and K are delimited by a vertical dashed line.

These results conclusively show that precise asteroseismology of cool dwarfs is now possible down to at least the mid-K spectral type, effectively opening a new domain in observational asteroseismology. This development carries significant implications for stellar astrophysics. In particular, mode amplitudes are determined by a delicate balance between energy supply and mode damping, both directly connected to the turbulent velocity field associated with convection (Houdek & Dupret 2015). Measurement of oscillation modes in cool dwarfs will thus shed light on the dynamical coupling between pulsations and near-surface convection in a regime yet unexplored. Theoretical calculations have suggested a scaling of the amplitudes of solar-like oscillations in Doppler velocity of the form $v_{\rm osc} \propto (L/M)^s$ (Christensen-Dalsgaard & Frandsen 1983; Kjeldsen & Bedding 1995), where L and M denote the stellar luminosity and mass, and the exponent s is expected to lie in the range 0.7–1.5 (Houdek et al. 1999; Samadi et al. 2005, 2007). Recent observations suggest that, for K dwarfs, mode amplitudes favor the upper bound of the predicted range for the exponent s (Campante et al. 2024; Hon et al. 2024; Li et al. 2025a), consistent with a transition toward a steeper scaling as one moves from the G- into the K-dwarf regime, occurring at $T_{\rm eff} \sim 5300$ K (see also Verner et al. 2011, where a negative $ds/dT_{\rm eff}$ gradient was measured, based on a large ensemble of main-sequence and subgiant *Kepler* stars). This emerging picture underscores the need for a deeper investigation into the physical origin of mode-amplitude scaling in the K-dwarf regime. Moreover, characterization of this scaling is key to accurately estimating the asteroseismic yield of the upcoming PLAnetary Transits and Oscillations of stars (PLATO; Goupil et al. 2024; Rauer et al. 2025) mission, whose P1 and P2 ("bright"), as well as P5 ("statistical") stellar samples extend down to spectral type K7.

Here, we report on the ongoing asteroseismic survey of bright (apparent visual magnitude $V < 6$) southern and equatorial K dwarfs (declination $\delta < +30°$) with ESPRESSO, presenting re-

cent observational campaigns on GJ 570 A (K4 V) and GJ 783 A (K2.5 V). We are able to detect and measure solar-like oscillations in the EPRV data of both stars. These stars thus join a still sparse but growing sample of seismic K dwarfs (see Fig. 1), enhancing the statistical basis for studies of convection–pulsation coupling. The remainder of the paper is organized as follows. Section 2 describes the ESPRESSO observations of GJ 570 A and GJ 783 A and the data reduction procedure used to obtain the RV time series. The spectroscopic determination of the stellar atmospheric parameters and chromospheric emission is presented in Sect. 3. A detailed asteroseismic analysis follows in Sect. 4. In Sect. 5, we place the measured oscillation amplitudes of GJ 570 A and GJ 783 A in a broader context and highlight the tension between the empirical mode-amplitude scaling for K dwarfs and predictions from 3D convection simulations. Section 6 summarizes and discusses the results.

2. Observations and data reduction

GJ 570 A and GJ 783 A are nearby ($d \sim 6$ pc), fifth-magnitude dwarfs of spectral type K4 and K2.5, respectively. GJ 570 A (HD 131977, HIP 73184, HR 5568, TIC 287157634) is the primary component of a quadruple system that further comprises an M1.5 V–M3 V close binary and a widely separated late-T brown dwarf (Burgasser et al. 2000). It is a BY Draconis-type variable, with variable star designation KX Librae (Samus et al. 2017). GJ 783 A (HD 191408, HIP 99461, HR 7703, TIC 1991380115) is a metal-poor star and the primary in a wide binary system with an M4 V companion (Allen et al. 2000). Table 1 compiles the stellar properties of GJ 570 A and GJ 783 A.

GJ 570 A and GJ 783 A are both part of the ExEP HWO Precursor Science Stars list (Mamajek & Stapelfeldt 2024) compiled by the NASA Exoplanet Exploration Program (ExEP), being among the best targets for a systematic imaging survey of habitable zones by the future Habitable Worlds Observatory (HWO). Both stars have been observed by TESS in 20-second cadence. GJ 783 A was included in the TESS Luminaries sample (Lund et al. 2025), based on Sector 67 data, and we have since reprocessed the data in the same manner to include Sector 94. Similarly, GJ 570 A was processed following Lund et al. (2025), based on Sector 91 data. In neither case did we detect solar-like oscillations in the TESS photometry. We note, however, that both stars will be observed again by TESS in Sector 105 (GJ 783 A) and Sector 115 (GJ 570 A).

We observed GJ 570 A (GJ 783 A) for five (six) consecutive nights with ESPRESSO in May (September) 2024. Observations were carried out in single-Unit Telescope (single-UT) high-resolution mode (1×1 binning, fast readout; median resolving power $R \approx 138{,}000$). The GJ 570 A campaign was initially scheduled for six nights, but the first night and the latter half of the fourth (or third effective) night were lost to high winds and overcast skies, during which the telescope remained closed, resulting in five usable nights of data. The remainder of the campaign was affected by extended periods of thin and thick cirrus, as well as occasional strong winds. In contrast, weather conditions during the GJ 783 A campaign were considerably more favorable, with photometric or mostly clear skies throughout. The average nightly seeing[1] varied from 0.″59–1.″28 (0.″53–0.″86) for GJ 570 A (GJ 783 A).

[1] Normalized to an airmass of one and to a wavelength of 500 nm (V band).

Table 1: Stellar properties of GJ 570 A and GJ 783 A.

	GJ 570 A		**GJ 783 A**	
Parameter	Value	Source	Value	Source
Basic data				
Sp. Type	K4 V	1	K2.5 V	1
V (Johnson)	5.72 [a]	2, 3	5.32	3
$B-V$ (Johnson)	1.02	3	0.87	3
δ (°)	−21.42	4	−36.11	4
$v_{\rm rad}$ (km s^{-1})	26.75 ± 0.12	4	−129.27 ± 0.12	4
d (pc) [b]	$5.885^{+0.002}_{-0.002}$	5	$6.011^{+0.004}_{-0.003}$	5
Spectroscopy				
$T_{\rm eff}$ (K)	4629 ± 123	6	4854 ± 83	6
[Fe/H] (dex)	−0.04 ± 0.07	6	−0.63 ± 0.06	6
[α/Fe] (dex)	0.04 ± 0.07	6	0.22 ± 0.06	6
log g (dex)	4.54 ± 0.07	6	4.49 ± 0.05	6
log $R'_{\rm HK}$ (dex)	−4.648 ± 0.009	6	−5.034 ± 0.003	6
Interferometry				
R ($R_\odot$)	0.715 ± 0.009	7	···	···
Asteroseismology				
$\Delta\nu$ (μHz)	197.29 ± 0.22	6	191.48 ± 0.04	6
$\delta\nu_{02}$ (μHz)	11.64 ± 0.73	6	12.48 ± 0.32	6
ε	1.328 ± 0.027	6	1.517 ± 0.004	6
$\nu_{\rm max}$ (μHz)	4705 ± 105	6	4455 ± 70	6
$v_{\rm osc,max}$ (cm s^{-1})	2.57 ± 0.52	6	4.90 ± 0.81	6
Frequency modeling				
M ($M_\odot$)	0.69 ± 0.02	6	0.69 ± 0.01	6
R ($R_\odot$)	0.689 ± 0.006	6	0.697 ± 0.005	6
$t_{\rm age}$ (Gyr)	8.9 ± 2.0	6	9.0 ± 0.8	6

Notes. [(a)] Magnitude at maximum brightness (BY Draconis-type variable). [(b)] Median of the geometric distance posterior.

References. (1) Gray et al. (2006); (2) Samus et al. (2017); (3) ESA (1997); (4) Gaia Collaboration et al. (2023); (5) Bailer-Jones et al. (2021); (6) This work; (7) Rains et al. (2020).

We obtained $N = 2369$ (2133) spectra[2] for GJ 570 A (GJ 783 A) using a fixed exposure time of 25 s and a median cadence of $\Delta t \sim 61$ s between exposures, corresponding to a Nyquist frequency of $\nu_{\rm Nyq} = 1/(2\Delta t) \sim 8.2$ mHz. The spectra were reduced using the ESPRESSO Data Reduction Software (DRS; Pepe et al. 2021) and RV time series[3] were derived via cross-correlation, similarly to Campante et al. (2024). The resulting RV time series are displayed in the upper subpanels of Fig. 2. These have been detrended by applying a high-pass filter to the raw time series, performed night by night using a triangular smoothing function with a 1.2-hour cutoff. This was done to remove slow modulations and intranight trends, thereby isolating the high-frequency signals of interest. The lower subpanels of Fig. 2 show the photon-noise-limited RV precision per data

[2] After discarding spectra for which the atmospheric dispersion correction failed, we were left with $N = 2250$ (2125) usable RV data points for GJ 570 A (GJ 783 A).

[3] Raw RV time series can be downloaded for both targets from this Zenodo repository.

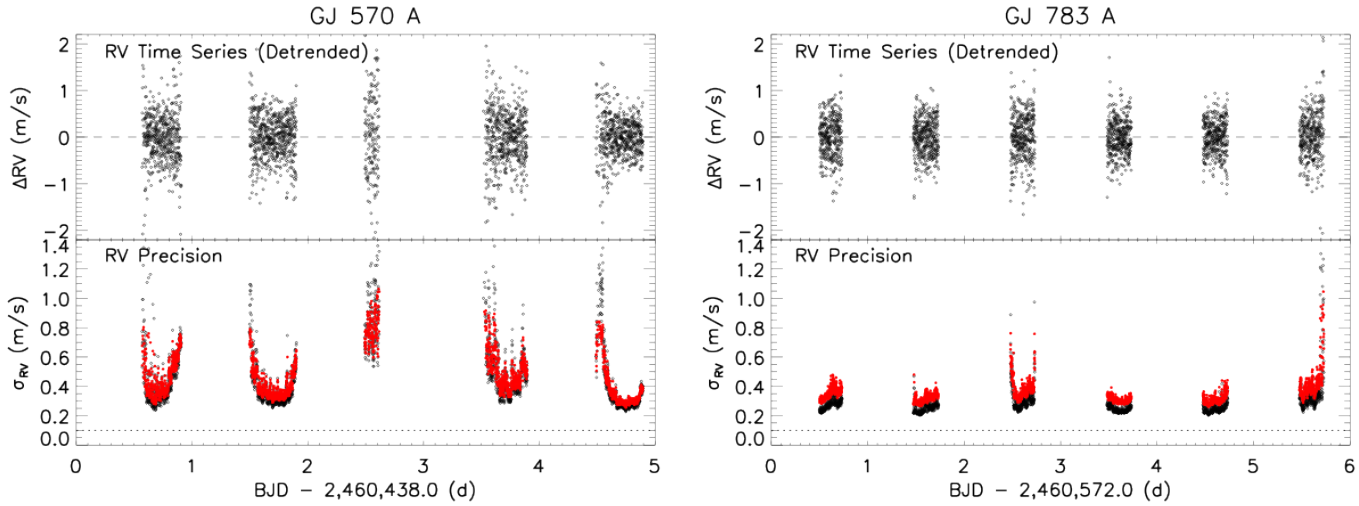

Fig. 2: Radial-velocity time series from ESPRESSO observations of GJ 570 A (left) and GJ 783 A (right). *Upper subpanels:* Detrended RV time series (see text for details). *Lower subpanels:* Internal RV precision as returned by the ESPRESSO DRS (open black diamonds) and recalibrated measurement uncertainties (filled red circles; see Sect. 4.1). Horizontal dotted lines mark the instrumental noise floor of 10 cm s^{-1} quoted by Pepe et al. (2021).

point, $\sigma_{\rm RV}$, as returned by the ESPRESSO DRS (open black diamonds), with average values of $\langle\sigma_{\rm RV}\rangle = 46$ cm s^{-1} for GJ 570 A and 29 cm s^{-1} for GJ 783 A. The corresponding root-mean-square (rms) scatter of the detrended RV time series is 54 cm s^{-1} (45 cm s^{-1}), exceeding the photon noise in both cases. This excess is attributed to the presence of solar-like oscillations as well as residual instrumental noise.

3. Spectroscopy

3.1. Stellar atmospheric parameters

Estimation of the effective temperature, $T_{\rm eff}$, surface gravity, $\log g$, and metallicity, [Fe/H], was performed using the `ARES` + `MOOG` method, described in detail in Santos et al. (2013); Sousa (2014); Sousa et al. (2021). We used the Automatic Routine for line Equivalent widths in stellar Spectra[4] (`ARES`; Sousa et al. 2007, 2015) to measure the equivalent widths of lines in co-added ESPRESSO spectra. Since both stars are cooler than 5200K, we adopted the line list introduced by Tsantaki et al. (2013), which is well suited for K dwarfs. The best-fit spectroscopic parameters were determined by employing a minimization procedure to enforce ionization and excitation equilibrium. This procedure used a grid of Kurucz model atmospheres (Kurucz 1993) and the latest version of the `MOOG` (Sneden 1973) radiative transfer code. Moreover, we followed the procedure described in Sousa et al. (2021) to derive a trigonometric $\log g$ by combining the spectroscopic $T_{\rm eff}$ with *Gaia* parallax and photometry (Gaia Collaboration et al. 2023), which provides a more accurate estimate than the purely spectroscopic $\log g$. We list the trigonometric $\log g$ in Table 1, along with $T_{\rm eff}$ and [Fe/H].

Based on the derived atmospheric parameters, we determined the abundances of Mg, Si, and Ti using a classical curve-of-growth analysis (e.g., Adibekyan et al. 2012, 2015). As in the stellar parameter determination, we used `ARES` to measure the equivalent widths of the spectral lines of these elements, and employed a grid of Kurucz model atmospheres together with `MOOG` to convert the equivalent widths into abundances under the assumption of local thermodynamic equilibrium (LTE). Finally, we estimated the α-element to iron abundance ratio, [α/Fe], as a weighted mean of the individual Mg, Si, and Ti abundances, using the inverse squared abundance uncertainties as weights (see Table 1).

For completeness, we also applied the same procedure to high-quality ESPRESSO spectra of ϵ Indi, which had been previously analyzed by our team in Campante et al. (2024), but without a homogeneous derivation of its atmospheric parameters. Using the methodology described above, we determined $T_{\rm eff} = 4581 \pm 130$ K, $\log g = 4.51 \pm 0.08$ dex, [Fe/H] $= -0.18 \pm 0.07$ dex, and [α/Fe] $= 0.00 \pm 0.08$ dex for this star.

3.2. Chromospheric emission

To estimate the mean activity level and investigate possible long-term trends, we supplemented the single-epoch ESPRESSO observations with archival HARPS data (Gomes da Silva et al. 2021). The HARPS data span from 2004 to 2012 for GJ 570 A, and from 2003 to 2008 for GJ 783 A. We extracted the S-index from the Ca II H&K lines (Duncan et al. 1991) using `ACTIN 2`[5] (Gomes da Silva et al. 2018, 2021), and computed the chromospheric emission ratio, $\log R'_{\rm HK}$, employing the `pyrhk`[6] package and the methodology outlined in Gomes da Silva et al. (2021). For each instrument, we performed an iterative 3σ clipping on the $\log R'_{\rm HK}$ time series to remove outliers before binning the data. The retained measurements were binned into 26 (HARPS) and 5 (ESPRESSO) observing nights for GJ 570 A, and 22 (HARPS) and 6 (ESPRESSO) nights for GJ 783 A. We searched for significant periodicities in the HARPS time series of both stars using a periodogram analysis (Zechmeister & Kürster 2009), but found no signals with false-alarm probabilities below 10%.

We next evaluated the mean activity levels, computing the weighted mean of $\log R'_{\rm HK}$ for each instrument separately. The associated uncertainties were estimated as the standard errors on the mean. For GJ 570 A, the chromospheric emission ratios derived from HARPS and ESPRESSO are nearly identical, with

[4] `https://github.com/sousasag/ARES`

[5] `https://github.com/gomesdasilva/ACTIN2`

[6] `https://github.com/gomesdasilva/pyrhk`

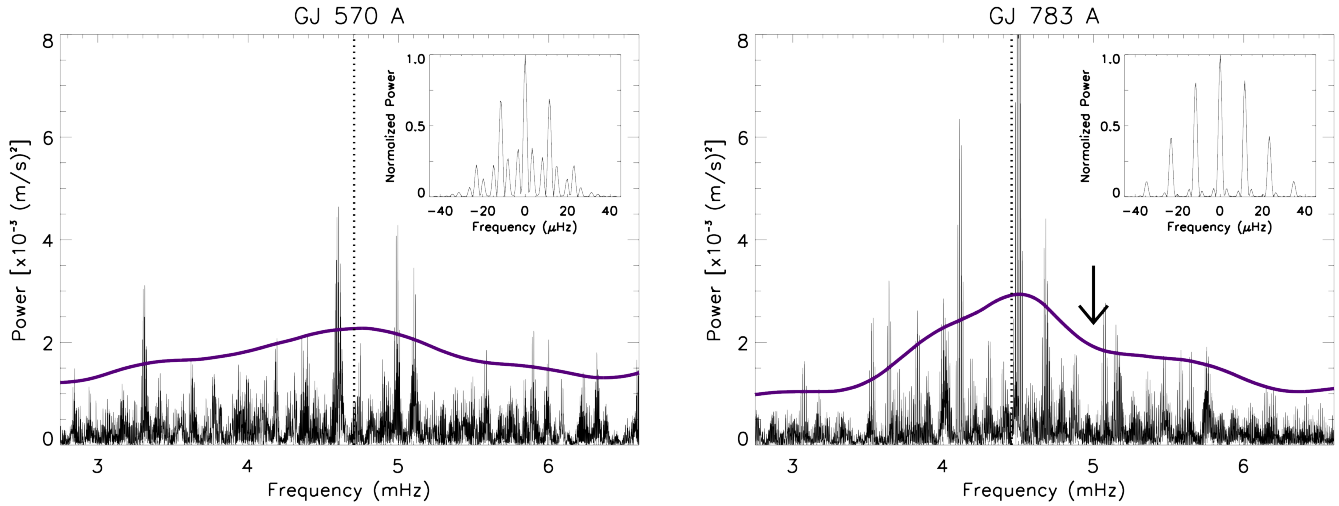

Fig. 3: Power spectra of GJ 570 A (left) and GJ 783 A (right), shown oversampled for clarity. Excess power from solar-like oscillations is visible in both panels, centered slightly below 5 mHz (vertical dotted lines mark the estimated $\nu_{\rm max}$). Smoothed power spectra, scaled by a factor of five, are overplotted to highlight this excess (thick dark purple curves). These smoothed curves are intended for visualization and differ from the heavily smoothed power spectra computed in Sect. 5.1. The arrow marks a dip in the oscillation power of GJ 783 A (see Sect. 5.2). Insets display the spectral windows, showing prominent sidelobes at multiples of $\pm 11.57\,\mu$Hz, or ± 1 d^{-1}, resulting from the single-site nature of the observations.

$\log R'_{\rm HK} = -4.649 \pm 0.005$ dex and -4.648 ± 0.009 dex, respectively. This consistency suggests that GJ 570 A may have maintained a stable activity level across the two-decade interval between 2004 and 2024. In contrast, for GJ 783 A, the HARPS data yield $\log R'_{\rm HK} = -4.983 \pm 0.003$ dex, whereas the more recent ESPRESSO observations indicate a lower activity level of $\log R'_{\rm HK} = -5.034 \pm 0.003$ dex, pointing to a possible long-term decline in chromospheric activity between the 2003–2008 and 2024 epochs. Overall, these activity levels indicate that GJ 570 A is a moderately active star, lying close to the Vaughan–Preston gap (Vaughan & Preston 1980), while GJ 783 A resides near the peak of the inactive-star distribution (Henry et al. 1996).

4. Asteroseismology

4.1. Oscillation frequencies

Power spectra of the detrended RV time series were computed based on the Lomb–Scargle periodogram (Lomb 1976; Scargle 1982), with measurement uncertainties adopted as statistical weights, i.e., $w_i = 1/\sigma^2_{{\rm RV},i}$ (Frandsen et al. 1995), where the subscript i denotes individual measurements. To further optimize the noise floor in the power spectra of both stars, these weights were adjusted to account for small fractions of bad data points (1.2% and 0.9% of the data points were removed for GJ 570 A and GJ 783 A, respectively) and for night-to-night variations in the noise level, following a well-established procedure (e.g., Bedding et al. 2004; Arentoft et al. 2008; Kjeldsen et al. 2025).

The resulting noise-optimized power spectra are shown in Fig. 3, revealing excess power from solar-like oscillations centered at frequencies slightly below 5 mHz (corresponding to typical oscillation periods of 3–4 minutes), although with a noticeably lower S/N for GJ 570 A (left panel). We estimated the frequency of maximum oscillation amplitude, $\nu_{\rm max}$, from heavily smoothed power spectra (see Sect. 5.1 for details), obtaining $\nu_{\rm max} = 4705 \pm 105\,\mu$Hz (GJ 570 A) and $4455 \pm 70\,\mu$Hz (GJ 783 A). Also apparent in the right panel of Fig. 3 is a dip in the oscillation power of the higher-S/N star GJ 783 A above $\nu_{\rm max}$. This feature is reminiscent of similar local minima reported in the oscillation spectra of α Centauri B (Kjeldsen et al. 2005) and HD 219134 (Li et al. 2025a). We return to a discussion of this feature in Sect. 5.2.

The white-noise level in the amplitude spectrum—defined as the square root of the power spectrum—was measured at high frequencies (6–8 mHz), yielding $\sigma_{\rm amp} = 1.51\,{\rm cm\,s^{-1}}$ for GJ 570 A and 1.29 cm s^{-1} for GJ 783 A. For comparison, the white-noise level reported for the ESPRESSO observations of ϵ Indi ($V = 4.69$) is 0.94 cm s^{-1} (Campante et al. 2024), consistent with its higher apparent brightness, while the number of data points, N, is very similar for all three targets. The recalibrated measurement uncertainties shown in the lower subpanels of Fig. 2 (filled red circles) reflect the adjusted weights described above and were further scaled to reproduce the high-frequency noise level in the amplitude spectrum.

The observed oscillation modes are acoustic (p) modes of high radial order, n, and low angular degree, ℓ, with their frequencies well approximated by the asymptotic relation (Tassoul 1980):

$$\nu_{n,\ell} \simeq \Delta\nu \left(n + \frac{\ell}{2} + \varepsilon \right) - \delta\nu_{0\ell}\,, \tag{1}$$

where $\Delta\nu$ is the large frequency separation between modes of the same degree and consecutive order, scaling as the square root of the mean stellar density; the small frequency separations $\delta\nu_{0\ell}$ (e.g., $\delta\nu_{02}$) are measured between modes of different degree and adjacent orders, being sensitive to the sound-speed gradient near the core in main-sequence stars; and the dimensionless offset, ε, is determined by the reflection properties of the surface layers.

The presence of daily aliases in the power spectra of both stars (see corresponding spectral windows in the insets of Fig. 3), appearing at multiples of $\pm 11.57\,\mu$Hz, or ± 1 d^{-1}, around genuine peaks, greatly complicates the process of mode identification and extraction. Measurement of the $\delta\nu_{02}$ spacing is particularly challenging, as it is expected to take values very close to 1 d^{-1} for K dwarfs, based on stellar models (White et al. 2011a,b). To recover the true power spectra, we therefore deconvolved the observed power spectra using their spectral windows by means of the Gold deconvolution algorithm (Gold 1964), as implemented

Table 2: Oscillation frequencies of GJ 570 A.

n	ℓ	$\nu_{n,\ell}$ (μHz)	$\sigma(\nu_{n,\ell})$ (μHz)
22	0	4602.38	0.73
24	0	4996.98	0.75
24	1	5091.01	0.65
19	2	4195.93	0.76
20	2	4394.34	0.78
23	2	4985.14	0.71

Notes. Listed frequencies were corrected for the stellar line-of-sight Doppler velocity shift, which for this star amounts to approximately +0.4 μHz at $\nu_{\max}$.

by Morháč et al. (2003). A similar deconvolution strategy was employed by Li et al. (2025a) in the asteroseismic analysis of HD 219134. Figures 4(a), (b) and 5(a), (b) show the échelle diagrams of GJ 570 A and GJ 783 A, respectively, before and after deconvolution, revealing $\ell = 0$–2 power ridges (as well as $\ell = 3$ in the case of GJ 783 A). These power ridges are made even more apparent in Figs. 4(c) and 5(c), which display the collapsed (along the vertical direction) deconvolved échelle diagrams, thereby facilitating mode identification and enabling the estimation of guess frequencies for mode extraction.

We extracted the mode frequencies by simultaneously fitting sine waves at these guess frequencies to the RV time series, retaining only those modes with amplitudes exceeding 2.5 times the white-noise level, $\sigma_{\rm amp}$ (i.e., S/N > 2.5; see Figs. 4(d) and 5(d)). Given the short duration of the RV time series, the modes are only marginally resolved, which justifies the use of coherent sine-wave fits. This procedure resulted in a total of 6 and 24 modes being extracted for GJ 570 A and GJ 783 A, respectively, as listed in Tables 2 and 3. The listed frequencies were corrected for the stellar line-of-sight Doppler velocity shift following Davies et al. (2014), using the corresponding *Gaia* radial velocities, $v_{\rm rad}$ (Gaia Collaboration et al. 2023). Frequency uncertainties were estimated using the analytical expression (Toutain & Appourchaux 1994; Kjeldsen & Bedding 2012):

$$\sigma(\nu) \approx 0.44\,\sigma_{\rm amp}\,a^{-1}\sqrt{T_{\rm obs}^{-2}+\tau^{-2}}\,, \tag{2}$$

where a is the mode amplitude, $T_{\rm obs}$ is the effective observing duration, and τ is the mode lifetime. In the uncertainty calculation, we assumed a conservative mode lifetime of 3 days (cf. Campante et al. 2024). In principle, the mode lifetime can be constrained observationally by measuring the scatter of the radial-mode frequencies about their power ridge in the échelle diagram and comparing it with simulations (e.g., Bedding et al. 2004; Kjeldsen et al. 2005). We attempted such an analysis for the higher-S/N star GJ 783 A; however, the measured scatter is too small to yield a robust lower limit on τ. Finally, we fitted Eq. (1) to both frequency sets to estimate the asymptotic parameters $\Delta\nu$, $\delta\nu_{02}$, and ε (see Table 1). Owing to the limited number of extracted modes for the lower-S/N star GJ 570 A, the corresponding $\delta\nu_{02}$ and ε values should be regarded as tentative, though they remain broadly consistent with stellar model predictions (cf. Campante et al. 2024); note that a small offset in ε relative to the models is expected due to the surface effect (e.g., Kjeldsen et al. 2008b; Ball & Gizon 2014).

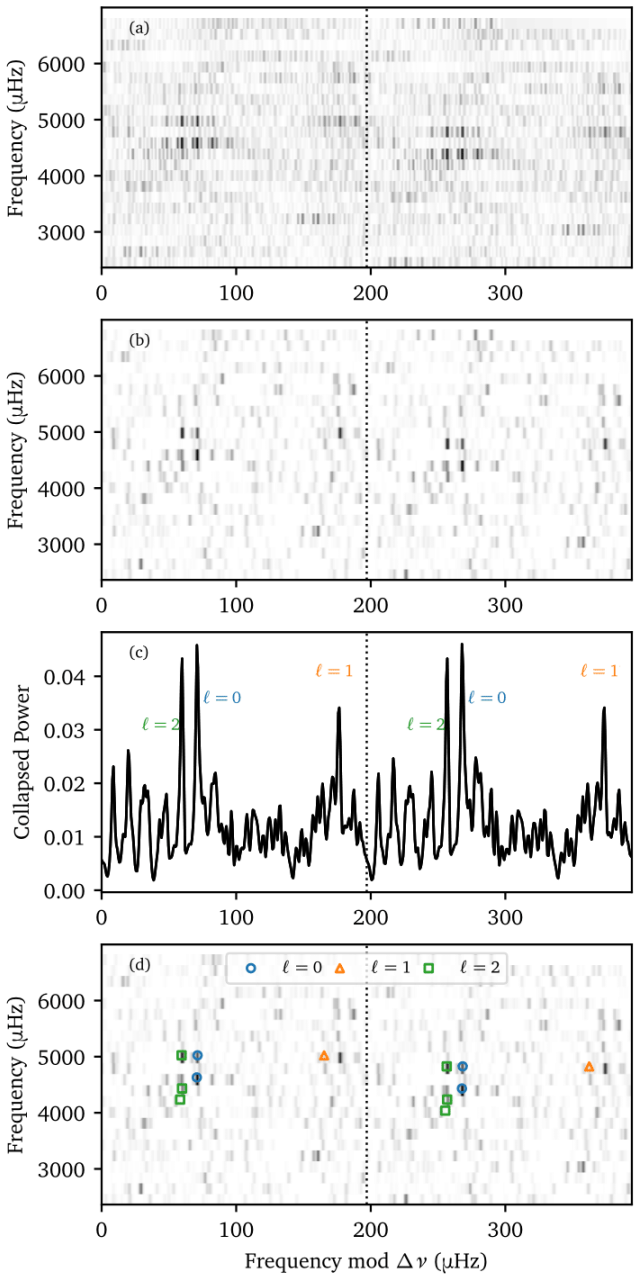

Fig. 4: Mode identification and extraction for GJ 570 A (see text for details). *Panel (a):* Replicated échelle diagram of the observed power spectrum. *Panel (b):* Replicated échelle diagram of the deconvolved power spectrum. *Panel (c):* Collapsed (vertically) deconvolved échelle diagram, with power ridges labeled by their corresponding angular degree. *Panel (d):* Same as panel (b), but highlighting the extracted modes. Vertical dotted lines indicate the estimated $\Delta\nu$.

4.2. Frequency modeling

We estimated the mass, M, radius, R, and age, $t_{\rm age}$, of GJ 570 A and GJ 783 A through frequency modeling (see Table 1). A detailed description of the modeling framework will be provided in Costa et al. (in prep.), and a summary is given below.

We employed a grid of stellar models computed with version r24.08.1 of Modules for Experiments in Stellar Astrophysics (`MESA`; Paxton et al. 2019). Stellar evolutionary tracks were initiated on the pre-main sequence when the central temperature reached 4×10^5 K and were evolved until the end of the main

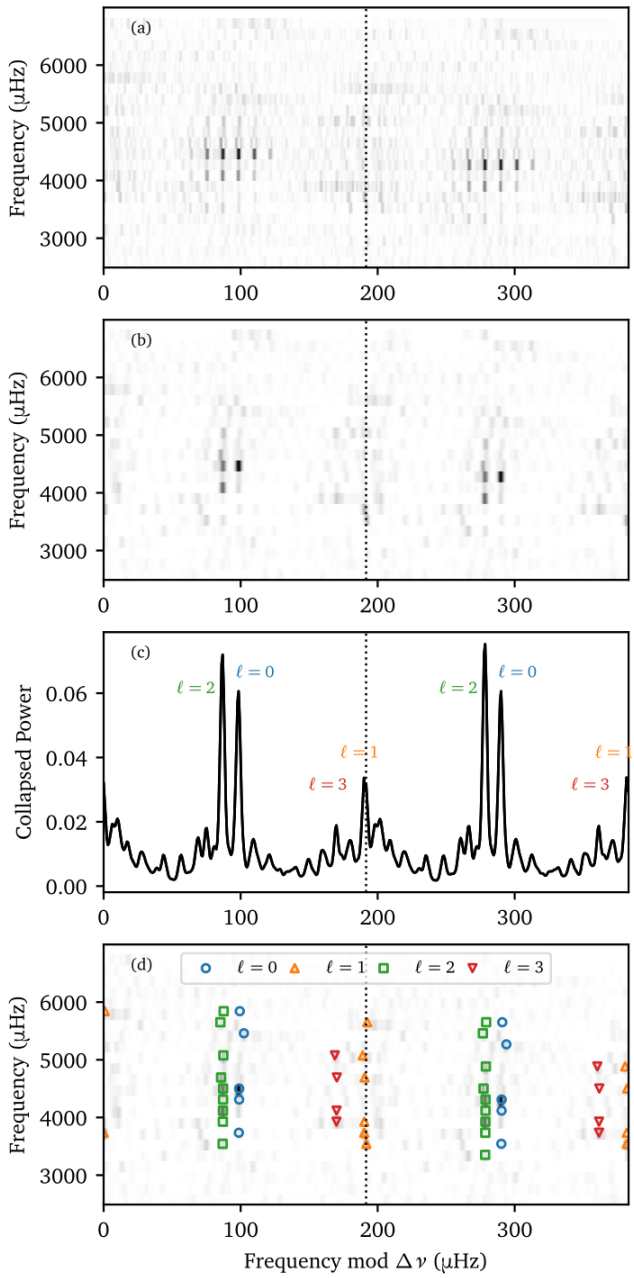

Fig. 5: Mode identification and extraction for GJ 783 A (see text for details). *Panels (a)–(d):* Replicated observed and deconvolved échelle diagrams, collapsed power, and extracted modes, respectively, with vertical dotted lines indicating the estimated $\Delta\nu$. The panels are arranged in the same format as in Fig. 4 for GJ 570 A. We note the lower-than-expected power ratio between the $\ell = 1$ and $\ell = 0$ ridges in panel (c) (e.g., Kjeldsen et al. 2008a), which we attribute to the stochastic nature of the oscillations.

sequence, defined as the point where the central hydrogen mass fraction dropped below 10^{-4}. The grid was constructed by varying the stellar mass, the initial metal fraction, $Z_{\rm init}$, and the mixing-length parameter, $\alpha_{\rm MLT}$, which were treated as free parameters. The mass ranged from 0.60 to 1.15 $M_\odot$ in steps of 0.01 $M_\odot$, $Z_{\rm init}$ ranged from 0 to 0.033 in steps of 0.001 (increasing to 0.002 in parts of the grid), and $\alpha_{\rm MLT}$ ranged from 1.0 to 3.0 in steps of 0.2.

We adopted the solar chemical mixture of Asplund et al. (2009). The initial helium fraction, $Y_{\rm init}$, was determined from a linear helium enrichment law, using the solar-calibrated helium-to-heavy element enrichment ratio from Grid A of Moedas et al. (2022), whose input physics are similar to ours. Convection was treated using a time-dependent formulation based on the model of Kuhfuss (1986). Nuclear reaction rates were taken from the standard `MESA` compilation, which combines rates from NACRE (Angulo 1999) and JINA REACLIB (Cyburt et al. 2010). Opacities were taken from the OPAL tables (Iglesias & Rogers 1996), supplemented at low temperatures by the tables of Ferguson et al. (2005). Furthermore, we employed the default blended equation of state in `MESA` and adopted a gray Eddington T–τ relation (Eddington 1926) to treat the atmospheric boundary condition. The models also included element diffusion through gravitational settling (Thoul et al. 1994); however, the effects of rotation, convective overshoot, and magnetic fields were neglected. For each model in the grid, we computed oscillation frequencies for modes of angular degree $\ell = 0$–3 using the `GYRE` (v7.2.1; Townsend & Teitler 2013) stellar oscillation code.

Model optimization was performed with Asteroseismic Inference on a Massive Scale (`AIMS`; Rendle et al. 2019), which employs Bayesian statistics and a Markov Chain Monte Carlo (MCMC) sampler to identify the best-fitting models within a predefined grid. As observational constraints, we used the mode frequencies listed in Tables 2 and 3, together with the corresponding effective temperature and metallicity from Table 1. Each mode frequency was assigned the same weight as a classical constraint. To correct mode frequencies for the surface effect, we applied the two-term prescription of Ball & Gizon (2014). For GJ 570 A, the inferred surface correction was found to have a

Table 3: Oscillation frequencies of GJ 783 A.

n	ℓ	$\nu_{n,\ell}$ (μHz)	$\sigma(\nu_{n,\ell})$ (μHz)
18	0	3736.72	0.72
21	0	4311.34	0.57
22	0	4502.88	0.52
27	0	5463.70	0.74
29	0	5843.65	0.56
17	1	3638.21	0.50
18	1	3828.19	0.45
19	1	4019.73	0.52
23	1	4785.89	0.64
25	1	5167.40	0.69
28	1	5745.15	0.66
16	2	3533.45	0.52
18	2	3916.53	0.70
19	2	4108.07	0.36
20	2	4299.61	0.65
21	2	4491.15	0.41
22	2	4681.13	0.44
24	2	5065.77	0.64
27	2	5638.04	0.77
28	2	5831.92	0.53
18	3	3999.40	0.46
19	3	4190.94	0.63
22	3	4765.56	0.72
24	3	5147.07	0.72

Notes. Listed frequencies were corrected for the stellar line-of-sight Doppler velocity shift, which for this star amounts to approximately $-2.0\,\mu$Hz at $\nu_{\rm max}$.

negative sign, contrary to expectation; we therefore constrained the correction to be positive, which effectively resulted in a negligible surface term for this star. Finally, we accounted for the α-enhancement of GJ 783 A by scaling its metallicity following the prescription of Salaris et al. (1993), and used the resulting value as input.

To account for potential systematic effects associated with the optimization procedure, we repeated the analysis using alternative optimization configurations. Specifically, we performed additional runs adopting (i) an alternative weighting scheme, in which the set of mode frequencies and the set of classical constraints were each assigned equal total weight, and (ii) the surface correction of Sonoi et al. (2015). For GJ 783 A, all combinations of these configurations were explored. For GJ 570 A, however, runs involving alternative surface corrections were not considered, since the constrained sign of the surface term led to a negligible correction. The uncertainties reported in Table 1 were obtained by adding in quadrature the formal uncertainties from the reference run and the standard deviation of the parameter estimates across all runs for each star.

The radius of GJ 570 A derived from frequency modeling is 3.6% smaller than the interferometric radius (see Table 1), corresponding to a 2.4σ difference. This offset is consistent with the well-known tendency of stellar models to underestimate the radii of K and M dwarfs by typically ∼5% relative to empirical measurements from eclipsing binaries and interferometry (e.g., Boyajian et al. 2012; Feiden & Chaboyer 2012, and references therein). Similar discrepancies have also been reported for individual K dwarfs at comparable or higher significance (e.g., Li et al. 2025a). To investigate this issue further, Costa et al. (in prep.) present the first attempt at systematically modeling an ensemble of seismic K dwarfs with published interferometric radii, testing the impact of different physical assumptions.

As GJ 570 A is part of a well-studied multiple system hosting the benchmark T dwarf GJ 570 D, its age has been constrained through several independent diagnostics in the literature. The seismic age derived here, 8.9 ± 2.0 Gyr, is significantly older than most previous estimates. Early activity and kinematic indicators suggest that the system is older than ∼2 Gyr and belongs to the Galactic disk, implying an approximate upper limit of ∼10 Gyr (Burgasser et al. 2000). However, subsequent estimates based on chromospheric activity, X-ray emission, and rotation generally favored substantially younger ages, typically in the range 1–5 Gyr (Geballe et al. 2001; Liu et al. 2007). Analyses of the brown-dwarf companion GJ 570 D using evolutionary models likewise yielded ages of 3–5 Gyr, with some preference toward the older end of this interval (Saumon et al. 2006; Phillips et al. 2020). The seismic estimate therefore lies above the commonly adopted upper bound of ∼5 Gyr and is in tension with most age indicators, although it remains formally compatible with the broader kinematic upper limit. This discrepancy may reflect systematic uncertainties affecting both stellar-model ages and empirical age diagnostics for late-type field stars.

5. Oscillation amplitudes: observations versus simulations

5.1. Empirical mode-amplitude scaling relation

The amplitudes of individual oscillation modes are affected by the stochastic nature of the excitation and damping. To measure oscillation amplitudes in a way that is independent of these effects, we adopted the procedure introduced by Kjeldsen et al. (2005, 2008a). Briefly, the power spectra were heavily smoothed

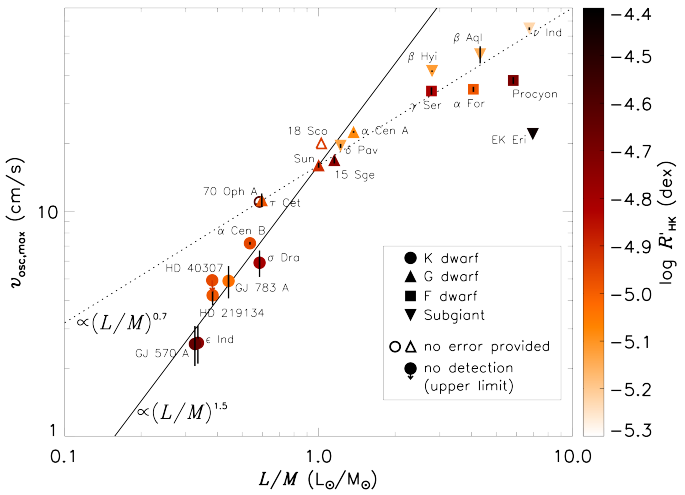

Fig. 6: Maximum amplitude per radial mode, $v_{\rm osc,max}$, as a function of L/M for GJ 570 A, GJ 783 A, the Sun, and a number of FGK dwarfs and subgiants with published Doppler velocity measurements. Data points are color-coded according to the chromospheric emission ratio, $\log R'_{\rm HK}$. Two scalings of the mode amplitude are shown, differing in terms of the exponent s ($s = 0.7$, dotted curve; $s = 1.5$, solid curve).

by convolution with a Gaussian kernel of full width at half maximum (FWHM) equal to $4\Delta\nu$, then converted to power density—defined as the power spectrum multiplied by the effective observing duration ($T_{\rm obs}$). We next subtracted the background (white) noise, and finally multiplied the result by $\Delta\nu/c$ and took the square root. Following Kjeldsen et al. (2008a), we used $c = 4.09$, which represents the effective number of modes per order for full-disk velocity observations, normalized to the amplitudes of radial modes. This procedure yields a smooth oscillation amplitude envelope, which we refer to as the amplitude per radial mode. The resulting envelope peak amplitudes are $v_{\rm osc,max} = 2.57 \pm 0.52$ cm s^{-1} for GJ 570 A (comparable to the peak amplitude of 2.6 cm s^{-1} measured for ϵ Indi) and 4.90 ± 0.81 cm s^{-1} for GJ 783 A. The uncertainties in the oscillation amplitudes were estimated using a bootstrap approach. In each realization, the original power spectrum was multiplied by a synthetic noise spectrum following a χ^2 distribution with two degrees of freedom (Woodard 1984), and the oscillation amplitude was remeasured. The dispersion of the resulting amplitude estimates across all realizations was then adopted as the uncertainty.

Figure 6 shows the maximum amplitude per radial mode, $v_{\rm osc,max}$, as a function of L/M (expressed in units of $L_\odot/M_\odot$), color-coded according to the chromospheric emission ratio, $\log R'_{\rm HK}$, for a total of 21 stars—GJ 570 A, GJ 783 A, the Sun, and a number of FGK[7] dwarfs and subgiants with published Doppler velocity measurements. The amount of smoothing of the power spectrum affects the exact height of the smoothed oscillation amplitude envelope, and hence the estimate of $v_{\rm osc,max}$. Measurements for Procyon (Arentoft et al. 2008), τ Ceti (Teixeira et al. 2009), EK Eridani (Bonanno et al. 2019), ϵ Indi (Campante et al. 2024), σ Draconis (Hon et al. 2024), β Aquilae (Kjeldsen et al. 2025), HD 219134 (Li et al. 2025a), 15 Sagittae (Li et al. 2025b), and the remaining targets (see table 2 of Kjeldsen et al. 2008a) were obtained following the same procedure as described above. There are a few exceptions to this.

[7] Procyon and α Fornacis are moderately evolved F-type stars transitioning from the main sequence toward the subgiant branch, and are therefore often assigned an intermediate luminosity class (IV-V).

Table 4: Basic properties of 3D surface convection simulations. Simulations `t45g46m00`, `t46g46m00`, and `t48g45m05` were designed to model ϵ Indi, GJ 570 A, and GJ 783 A, respectively. As $T_{\rm eff}$ is an emergent quantity of the 3D simulations that fluctuates over time, both its time-averaged mean and standard deviation are provided.

Simulation	`t45g46m00`	`t46g46m00`	`t48g45m05`
Standard simulations			
$T_{\rm eff}$ (K)	4571 ± 7	4669 ± 8	4854 ± 7
$\log g$ (dex)	4.62	4.57	4.55
[Fe/H] (dex)	0	0	−0.5
Numerical grids	$240^2 \times 260$	$240^2 \times 260$	$240^2 \times 254$
Time duration (h)	10	11.67	12.5
Sampling interval (s)	12	14	15
Horizontal size (Mm)	3.13	3.56	4.12
Vertical size (Mm)	1.79	2.06	2.47
Vertical grid spacing (km)	3.8–12.4	4.4–14.3	4.5–19.4
Artificial driving simulations			
Numerical grids	$120^2 \times 158$	$120^2 \times 158$	$120^2 \times 158$
Time duration (h)	50	46.67	50
Sampling interval (s)	12	14	15
Horizontal size (Mm)	3.13	3.56	4.12
Vertical size (Mm)	2.47	2.86	3.67
Vertical grid spacing (km)	7.7–24.7	8.7–28.5	8.9–38.8

The value plotted for 70 Ophiuchi A (Carrier & Eggenberger 2006) corresponds to the lower bound on the amplitudes of the highest detected mode peaks and has no associated uncertainty; an estimate of the mode amplitudes for the solar twin 18 Scorpii is given in Bazot et al. (2011), for which no uncertainty is reported; finally, a reanalysis of the ESPRESSO Guaranteed Time Observations (GTO) data for HD 40307 showed no p-mode detection (Campante et al. 2024), and so the plotted value is an upper limit. For the Sun, we adopt a more recent determination from Kjeldsen et al. (2025) obtained using the same procedure: the plotted value $v^{\odot}_{\rm osc,max} = 16.0 \pm 0.4$ cm s^{-1} was derived from observations with the Stellar Observations Network Group (SONG; Grundahl et al. 2007) and subsequently corrected to the mean solar activity level based on measurements from the Variability of solar IRradiance and Gravity Oscillations (VIRGO; Fröhlich et al. 1995) experiment. It is worth noting that the plotted $v_{\rm osc,max}$ values are effectively single-epoch determinations and therefore the quoted uncertainties do not account for possible variations induced by magnetic activity cycles (e.g., García et al. 2010); the Sun is a partial exception, in that the value has been corrected to the mean activity level, although it is likewise based on a single-epoch measurement.

The ratio L/M can be expressed as a ratio of atmospheric parameters via $L/M \propto T_{\rm eff}^4/g$, which we effectively used to compute the quantities along the x-coordinate (having adopted $T_{\rm eff,\odot} = 5777$ K and $g_\odot = 27402$ cm s^{-2}). Estimates of $T_{\rm eff}$ and $\log g$ for GJ 570 A, GJ 783 A, and ϵ Indi were taken from the spectroscopic analysis in Sect. 3.1. For the remaining stars, we adopted spectroscopic $T_{\rm eff}$ and $\log g$ values from the mean PASTEL catalog (Soubiran et al. 2022); except for Procyon and EK Eridani, which are not included in that compilation and for which we adopted parameters from the *Gaia*–ESO catalog (Hourihane et al. 2023) and Dall et al. (2010), respectively.

In Fig. 6, we show two scalings of the mode amplitude of the form

$$v_{\rm osc,max} \propto (L/M)^s = v^{\odot}_{\rm osc,max} \left(\frac{L/L_\odot}{M/M_\odot} \right)^s = v^{\odot}_{\rm osc,max} \left(\frac{T_{\rm eff}^4/T_{\rm eff,\odot}^4}{g/g_\odot} \right)^s , \quad (3)$$

corresponding to the extrema of the theoretical range in s, namely, $s = 0.7$ and 1.5. A transition can be clearly seen, with decreasing L/M, from an $\sim (L/M)^{0.7}$ scaling to a steeper $\sim (L/M)^{1.5}$ scaling, occurring near the G/K-dwarf boundary at $T_{\rm eff} \sim 5300$K. This provides compelling support for the trend previously suggested by Campante et al. (2024); Hon et al. (2024); Li et al. (2025a). In addition, the well-documented overestimation of predicted amplitudes for F-type stars is also apparent (e.g., see Kjeldsen & Bedding 2011, and references therein).

Measurements of $\log R'_{\rm HK}$ for GJ 570 A, GJ 783 A, and ϵ Indi were taken from Sect. 3.2 and Campante et al. (2024, for ϵ Indi). These are the only stars in the sample for which single-epoch chromospheric activity measurements were used; these measurements are strictly contemporaneous with the asteroseismic data. For the Sun, we adopted a mean chromospheric emission ratio averaged over four consecutive solar cycles (Mamajek & Hillenbrand 2008). For the remaining stars, values of $\log R'_{\rm HK}$ were drawn from the homogeneous catalog of Gomes da Silva et al. (2021) whenever available, or from Boro Saikia et al. (2018) otherwise.

The fraction of magnetically active stars among K dwarfs is known to be higher than among G dwarfs (e.g., Jenkins et al. 2011; Gomes da Silva et al. 2021), and increased activity tends to suppress the amplitudes of solar-like oscillations (e.g., Chaplin et al. 2000, 2011; García et al. 2010; Bonanno et al. 2014; Campante et al. 2014; Crawford et al. 2025; Sayeed et al. 2025). We examined the relationship between L/M and $\log R'_{\rm HK}$ for the stars in our sample, and found a negative correlation that becomes more pronounced when excluding the overactive

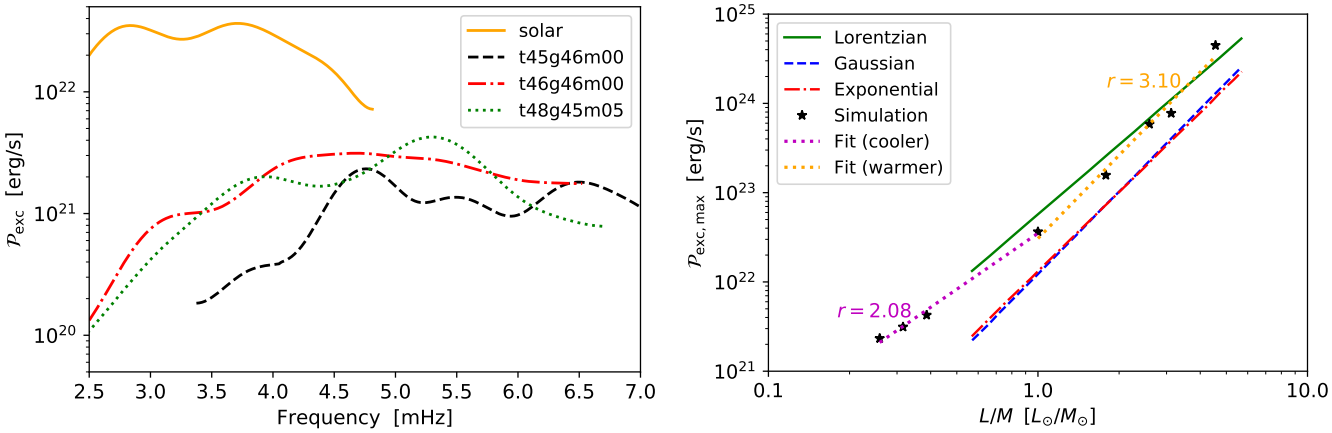

Fig. 7: *Left:* Energy injection rates, $\mathcal{P}_{\rm exc}$, of radial p modes as a function of frequency for the three K-dwarf models and a solar model (Zhou et al. 2019). The curves were smoothed to mitigate the impact of random fluctuations inherent to the simulations. *Right:* Maximum excitation rate, $\mathcal{P}_{\rm exc,max}$, as a function of L/M. Solid, dashed, and dash-dotted lines show the relations from Samadi et al. (2007, their fig. 6), with the labels "Lorentzian", "Gaussian", and "Exponential" indicating the different analytical turbulence models used in their calculations. Black star symbols represent results from 3D simulations: the three K-dwarf models listed in Table 4, and the solar model together with the warmer models taken from Zhou et al. (2020). Two separate fits to the simulation data are shown: the magenta dotted line is the linear regression of the three K-dwarf models and the solar model, while the orange dotted line corresponds to the linear regression for the warmer models, including the solar model.

subgiant EK Eridani. For this reduced sample, Spearman's rank correlation coefficient is $\rho = -0.43$ with a two-sided p-value of 0.06, indicating a moderate monotonic trend. A 68% bootstrap confidence interval for the correlation, $[-0.64, -0.17]$, remains entirely negative, indicating that the relationship is not driven by individual stars. This raises the possibility that higher activity levels among K dwarfs may contribute to the transition between amplitude scalings near the G/K-dwarf boundary shown in Fig. 6.

To assess whether chromospheric activity introduces an additional dependence in the amplitude scaling, we fitted the data with an extended relation of the form (e.g., see Campante et al. 2014; Crawford et al. 2025; Sayeed et al. 2025)

$$v_{\rm osc,max} = v^{\odot}_{\rm osc,max} \left(\frac{T^4_{\rm eff}/T^4_{\rm eff,\odot}}{g/g_\odot} \right)^s e^{\,u\left(\log R'_{\rm HK} - \log R'_{\rm HK,\odot}\right)}, \quad (4)$$

and compared it to the baseline scaling in Eq. (3). The fits were performed in logarithmic space using Monte Carlo propagation of the observational uncertainties in $v_{\rm osc,max}$, $T_{\rm eff}$, $\log g$, and $\log R'_{\rm HK}$, including conservative uncertainty floors for $T_{\rm eff}$, $\log g$, and $\log R'_{\rm HK}$ to account for heterogeneous literature sources, and adopting 10% uncertainties for the two stars lacking reported uncertainties in $v_{\rm osc,max}$. Restricting the analysis to the 19 stars with measured amplitudes (the Sun, which sets the normalization, is excluded) yields a statistically improved fit according to the corrected Akaike Information Criterion (AICc) when including the activity term, together with a reduction in the weighted scatter of the relation. The fitted activity exponent is negative ($u = -0.88^{+0.39}_{-0.43}$), significant at the 2σ level and consistent with the expected suppression of oscillation amplitudes with increasing magnetic activity. However, the inclusion of the activity term does not reduce the residual offset between K dwarfs and G dwarfs, which characterizes the empirical break in amplitude scaling near the G/K-dwarf boundary; the distribution of the corresponding offset difference is symmetric about zero, indicating no meaningful change. We therefore find no clear evidence that magnetic activity contributes to the observed break in the scaling relation near the G/K-dwarf boundary, although a contribution cannot be ruled out given the limited sample size.

5.2. Tension with 3D surface convection simulations

To investigate the physical origin of the empirical mode-amplitude scaling for K dwarfs presented in the previous section, we conducted 3D surface convection simulations and assessed whether it can be reproduced from first-principles convection modeling. The velocity amplitude of radial p-mode oscillations can be estimated from 3D surface convection simulations by quantifying both the energy injection and damping rates, following the methodology described in Nordlund & Stein (2001); Stein & Nordlund (2001); Zhou et al. (2020). In short, the energy injection rate is computed from nonadiabatic pressure fluctuations predicted by the 3D simulations, whereas linear damping rates are quantified through so-called artificial driving simulations (see the appendix of Zhou et al. 2020), where a sinusoidal perturbation is applied at the bottom boundary of the simulation domain to artificially excite a radial oscillation to a large amplitude. Mode masses and eigenfunctions, which are required for the calculation of both quantities, are obtained from 1D stellar structure models that are patched to the mean 3D stratification following Zhou et al. (2019). Here, the 1D stellar structure models were computed using `MESA`, adopting the same setup as described in Sect. 4.2, and the best-fitting model was selected by matching the mean $T_{\rm eff}$ and $\log g$ of the 3D simulation.

Three 3D surface convection simulations were computed with the radiative-magnetohydrodynamics code `Stagger` (Nordlund & Galsgaard 1995; Collet et al. 2018; Stein et al. 2024), designed to model ϵ Indi, GJ 570 A, and GJ 783 A (see Table 4). The code is equipped with a realistic equation of state and a comprehensive collection of continuum and line opacities. All 3D models were constructed with detailed radiative transfer calculations but without magnetic fields. Basic properties of the simulations used to compute the energy injection rates are summarized in the upper section of Table 4. The mean $T_{\rm eff}$ values of the simulations are consistent with the spectroscopic measurements within uncertainties. The input $\log g$ values were determined from the measured $T_{\rm eff}$ and $\nu_{\rm max}$ according to the $\nu_{\rm max}$ scaling relation (Brown et al. 1991). The Asplund et al. (2009) metal mixture was adopted in all simulations, consistent with the stellar structure modeling in Sect. 4.2.

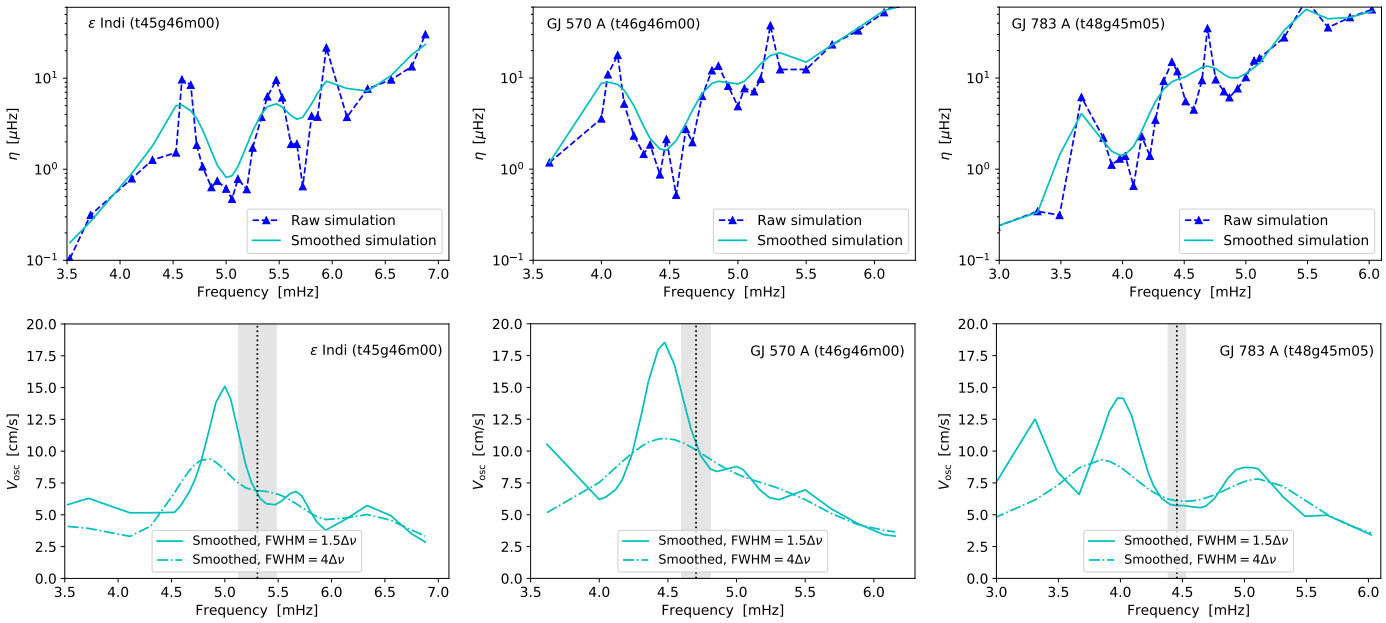

Fig. 8: *Upper panels:* Linear damping rates, η, of radial p modes as a function of frequency for the three K-dwarf models (blue triangles connected by dashed lines). The cyan solid curves represent smoothed versions of the raw simulation data. *Lower panels:* Corresponding smoothed (fluid) velocity amplitudes, $V_{\rm osc}$. The cyan solid and dash-dotted curves were obtained by smoothing with Gaussian kernels of FWHM $1.5\Delta\nu$ and $4\Delta\nu$, respectively. The $\nu_{\rm max}$ values measured in this work (see Table 1) and in Campante et al. (2024, for ϵ Indi) are indicated by vertical dotted lines, with associated uncertainties shown as gray bands.

Vertically, the simulations span the lower atmosphere, the photosphere, and the superadiabatic convective layers just below the surface, where convective turbulence and nonadiabatic effects responsible for mode excitation and damping are prominent. The highest vertical resolution was applied near optical depth unity to better capture the transition from the optically thick to the optically thin regime. The horizontal size of the simulations was determined based on the typical size of granules for the corresponding stellar parameters (Magic et al. 2013). The numerical resolution was halved for the artificial driving simulations (see lower section of Table 4), which were instead extended deeper into the stellar interior, and their temporal coverage was significantly increased, to improve the reliability of the predicted damping rates.

The energy injection rates, $\mathcal{P}_{\rm exc}$, of radial p modes for the three K-dwarf models and a solar model (Zhou et al. 2019) are shown in the left panel of Fig. 7. As a function of frequency, the energy injection rates exhibit a common pattern: $\mathcal{P}_{\rm exc}$ varies rapidly at low frequencies, reaches a broad plateau encompassing the frequency of maximum oscillation amplitude ($\nu_{\rm max}$), and decreases toward higher frequencies. Regarding the dependence of the energy injection on fundamental stellar parameters, Samadi et al. (2007) proposed a power-law relationship between the maximum excitation rate and the luminosity-mass ratio, $\mathcal{P}_{\rm exc,max} \propto (L/M)^r$. The corresponding quantities derived from our simulations are shown in the right panel of Fig. 7, where $\mathcal{P}_{\rm exc,max}$ is evaluated as the maximum of the smoothed excitation rate and L/M is computed from the mean $T_{\rm eff}$ and $\log g$ of the 3D model. As shown in the previous section, observed mode amplitudes exhibit a clear transition from an $\sim (L/M)^{0.7}$ scaling for warmer stars to a steeper $\sim (L/M)^{1.5}$ scaling for cooler stars, occurring near the G/K-dwarf boundary. Motivated by this change in scaling behavior, we performed two separate linear regressions of $\mathcal{P}_{\rm exc,max}$: one for stars with $L/M \leq L_\odot/M_\odot$, comprising the three K-dwarf models and the solar model, and another for $L/M \geq L_\odot/M_\odot$, comprising the solar model together with the warmer models studied by Zhou et al. (2020). For the warmer stars, the fitted exponent is $r \approx 3.1$. For the cooler stars, the corresponding exponent, $r \approx 2.1$, is smaller than those predicted by all three turbulence models considered by Samadi et al. (2007). We do not attempt a detailed quantitative interpretation of the fitted exponents, as the estimated $\mathcal{P}_{\rm exc,max}$ values are affected by random fluctuations in the simulations. Nevertheless, the 3D simulations suggest that energy injection into p modes decreases more slowly with decreasing L/M for stars cooler than the Sun, which is at odds with the steeper mode-amplitude decline inferred observationally for these stars.

The stability of an oscillation and its associated energy loss are characterized by the damping rate. For a given oscillation mode, the damping rate is determined by the density fluctuations induced by the oscillation, the pressure fluctuations, and the phase relationship between these two quantities. It is difficult to obtain reliable damping rates from the "standard" 3D simulations introduced above, whose density fluctuations contain contributions from both convection and oscillations. To overcome this limitation, we computed linear damping rates for radial oscillations following the method of Zhou et al. (2020), using simulations in which a radial oscillation is continuously driven at the bottom boundary of the simulation domain. The artificial driving produces a coherent oscillation with large amplitude, for which the density fluctuations predominantly arise from the oscillation. These "artificial driving" simulations were repeated at various frequencies to obtain damping rates, η, as a function of frequency (see upper panels of Fig. 8). Once the energy injection and damping rates have been quantified from the simulations, the velocity amplitude can be derived from the condition of energy balance (see lower panels of Fig. 8). We note that the velocity amplitude ($V_{\rm osc}$) displayed in Fig. 8 corresponds to the fluid velocity, whose absolute value is not directly comparable to the observed velocity amplitude ($v_{\rm osc}$). The two are instead

related by a projection factor (or spatial response function) that captures limb darkening and other geometrical effects associated with disk integration (e.g., see Christensen-Dalsgaard & Gough 1982; Kjeldsen et al. 2008a), which is not explicitly accounted for in the present analysis.

The precise value of $\nu_{\max}$ derived from the 3D simulations depends on the adopted smoothing of $V_{\rm osc}$ (see Fig. 8). Nevertheless, in line with previous studies (Zhou et al. 2019, 2020), the simulated $\nu_{\max}$ values show broad agreement in scale with observations, lying $\sim$ 5–10% below the observed values, indicating a systematic offset in excess of the formal observational uncertainties (~ 2–3σ for ϵ Indi and GJ 570 A, and $> 3\sigma$ for GJ 783 A). Figure 8 also reveals the systematic presence of local minima, bracketed by local maxima, in the predicted velocity amplitudes of all three K-dwarf models, most clearly visible in the curves smoothed with the narrower Gaussian kernel (see also Chaplin et al. 2007, where synthetic p-mode spectra of stars cooler than $\sim$ 5400 K exhibit two maxima). These amplitude minima correspond to local maxima in the damping-rate profiles. Observational support for this behavior is provided by the apparent dip above $\nu_{\max}$ in the oscillation power of GJ 783 A (see right panel of Fig. 3).

Owing to substantial frequency-dependent fluctuations in both the energy injection and damping rates, only a coarse estimate of the maximum velocity amplitude, $V_{\rm osc,max}$, can be derived. We identified $V_{\rm osc,max}$ as the maximum of the cyan dash-dotted curves in the lower panels of Fig. 8, which were obtained by smoothing the raw simulation data with a Gaussian kernel of FWHM $4\Delta\nu$, analogously to the treatment of the observed velocity amplitudes (see Sect. 5.1). The resulting estimates of $V_{\rm osc,max}$ for the three K-dwarf models and the solar model of Zhou et al. (2019) are shown in Fig. 9, together with a linear regression of $\log V_{\rm osc,max}$ against $\log(L/M)$, which yielded an exponent $s \approx 0.9$ (see Eq. 3). The maximum velocity amplitude for model `t48g45m05` lies slightly below the value predicted by the linear regression, which is likely attributable to its lower metallicity relative to the other models, leading to reduced oscillation amplitudes in the simulations (e.g., see Houdek et al. 1999; Samadi et al. 2010b,a). Although the absolute values of the predicted (fluid) velocities are not directly comparable to the observed values, their dependence on L/M can nevertheless be meaningfully compared with the observationally inferred scaling in Sect. 5.1. Strikingly, the 3D convection simulations are unable to recover the steep ($s \approx 1.5$) empirical mode-amplitude scaling of K dwarfs. This mismatch therefore highlights a clear tension between first-principles convection modeling and the observed amplitude behavior of solar-like oscillations in cool dwarfs.

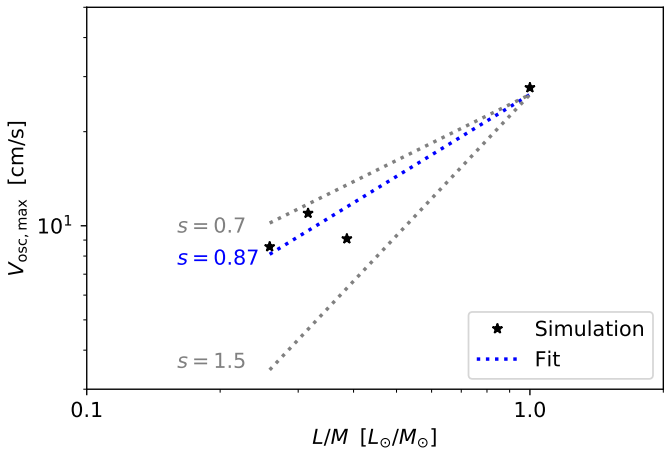

Fig. 9: Maximum (fluid) velocity amplitudes, $V_{\rm osc,max}$, as a function of L/M for the three K-dwarf models and a solar model (Zhou et al. 2019), shown as black star symbols. The blue dotted line is the linear regression of $\log V_{\rm osc,max}$ against $\log(L/M)$. The gray dotted lines indicate reference scalings with fixed exponents, $s = 0.7$ and $s = 1.5$.

6. Summary and discussion

To place our results in context, we briefly summarize the main findings before discussing the current limitations of our approach and outlining future directions:

- We carried out high-cadence ESPRESSO campaigns on GJ 570 A (K4 V) and GJ 783 A (K2.5 V), obtaining radial-velocity time series with white-noise levels of $\sim$ 1.3–1.5 cm s^{-1}, as measured at high frequencies in the amplitude spectra. The corresponding power spectra exhibit an excess consistent with solar-like oscillations in both stars. These detections add to the steadily expanding sample of seismic K dwarfs, strengthening the statistical basis for studies of convection–pulsation coupling.
- The oscillation power excess is centered slightly below 5 mHz in both targets, with individual modes identified for angular degrees $\ell = 0$–2 (and $\ell = 3$ in the case of GJ 783 A). In total, 6 modes were measured for GJ 570 A and 24 modes for GJ 783 A. The higher-S/N data for GJ 783 A additionally reveal an apparent dip in the oscillation power above $\nu_{\max}$, reminiscent of similar local minima reported for other K dwarfs.
- From heavily smoothed power spectra, we measured peak radial-mode amplitudes of 2.57 ± 0.52 cm s^{-1} for GJ 570 A and 4.90 ± 0.81 cm s^{-1} for GJ 783 A. These values help reveal a transition from an $\sim (L/M)^{0.7}$ scaling to a significantly steeper $\sim (L/M)^{1.5}$ dependence, occurring near the G/K-dwarf boundary toward decreasing L/M. This provides strong empirical support for the trend previously suggested by Campante et al. (2024); Hon et al. (2024); Li et al. (2025a). While oscillation amplitudes correlate with chromospheric activity, we find no clear evidence that magnetic activity contributes to the observed break in amplitude scaling, although a contribution cannot be ruled out with the present sample.
- State-of-the-art 3D surface convection simulations (including explicit calculations of excitation and linear damping rates) predict a maximum velocity-amplitude scaling $V_{\rm osc,max} \propto (L/M)^{0.9}$. The simulations thus fail to reproduce the steep empirical $(L/M)^{1.5}$ amplitude scaling observed for K dwarfs, revealing a clear tension between first-principles convection modeling and the measured amplitude behavior in cool dwarfs.

The discrepancy between predictions from 3D models and observations suggests that additional physical ingredients and/or limitations of the current modeling assumptions may play an important role, and warrants further investigation. We note that linewidths of individual oscillation modes, defined as $\Gamma = \eta/\pi = 1/(\pi\tau)$, are available for a few main-sequence stars with $T_{\rm eff} < 5500$ K as part of the *Kepler* LEGACY sample (Lund et al. 2017, their fig. 20). For these cool dwarfs, the observed mode linewidths at $\nu_{\max}$ are typically around 1 μHz, with some scatter, translating to damping rates of about 3 μHz at $\nu_{\max}$. As shown in Fig. 8, the simulated $\nu_{\max}$ values correspond to the primary

local minimum of the damping rate profile for all three 3D models. The smoothed $\eta(\nu_{\rm max})$ values are approximately 0.85, 1.67, and 1.45 μHz for `t45g46m00`, `t46g46m00`, and `t48g45m05`, respectively. This clearly indicates that our simulations underestimate mode damping by a factor of two or more, and consequently overestimate the oscillation amplitudes. This mismatch could stem from intrinsic uncertainties and limitations of the numerical approach used to estimate η, or may point to additional damping mechanisms not taken into account in our 3D simulations, such as magnetic fields.

It is reasonable to attribute this tension partly to the absence of magnetic fields in our convection simulations. It is known from both observations (Chaplin et al. 2000, 2011; García et al. 2010; Bonanno et al. 2014; Campante et al. 2014; Crawford et al. 2025; Sayeed et al. 2025) and convection simulations (Jacoutot et al. 2008; Kitiashvili et al. 2011) that magnetic fields suppress the amplitudes of p-mode oscillations, a behavior that is also supported by our results (Sect. 5.1). Because both ϵ Indi and GJ 570 A are more active than the Sun, as indicated by their chromospheric emission ratio $\log R'_{\rm HK}$, magnetoconvection simulations with appropriate field strengths would plausibly yield lower maximum velocity amplitudes for these stars and, consequently, a steeper fitted slope. Nevertheless, without detailed magnetohydrodynamical modeling, it cannot be determined within the framework of the present study to what extent magnetic suppression accounts for the tension between 3D simulations and observations.

Another complication arises from the difference between $V_{\rm osc,max}$ derived from the 3D simulations and the observed RV oscillation amplitudes. The former correspond to velocities evaluated at a fixed geometrical layer close to Rosseland optical depth unity, whereas the latter represent velocities sampled over the effective line-formation heights of the spectral lines used in the RV extraction. Although both refer to layers within the photosphere, many of the lines contributing to RV measurements are formed at smaller continuum optical depths, i.e., geometrically higher atmospheric layers, than the $\tau_{\rm Ross} \approx 1$ surface. Furthermore, the formation heights of spectral lines in the Sun differ from those in K dwarfs, implying that the fitted slope would change if synthesized RVs from detailed line-formation calculations were used instead of velocities at a fixed depth. For Fe I lines, which constitute a major set of lines in the ESPRESSO cross-correlation masks (Pepe et al. 2021), the same transition, at fixed iron abundance, generally exhibits a larger equivalent width in a K dwarf than in the Sun. This is primarily due to the higher fraction of neutral iron at lower effective temperatures, which increases the line opacity. As a result, these lines form at smaller continuum optical depths, corresponding to geometrically higher layers within the photosphere, in K dwarfs. Because oscillation velocity amplitudes increase with height in the atmosphere (e.g., Isaak et al. 1989; Baudin et al. 2005; Houdek 2006; Luhn et al. 2025), using velocities evaluated near $\tau_{\rm Ross} \approx 1$ likely underestimates the observed RV oscillation amplitudes, with the effect being stronger at lower L/M. It follows that incorporating line-formation effects would preferentially increase the modeled amplitudes of K dwarfs, thereby further flattening the inferred scaling of $V_{\rm osc,max}$ with L/M and yielding an exponent even smaller than that obtained from velocities evaluated at a fixed depth. An additional factor affecting the RV oscillation amplitudes is that different instruments rely on different spectral lines for RV measurements. Even for a given instrument, the set of lines used can vary from star to star. Consequently, it is not straightforward, even at a qualitative level, to assess the impact of adopting velocities from a fixed depth on the fitted slope s. A detailed synthesis of RV signals from simulations, using a method that resembles the observational procedure, is required to derive velocity amplitudes that are fully comparable with observations. Such an analysis lies beyond the scope of the present work but will be addressed in future studies.

Acknowledgements. Based on observations collected at the European Southern Observatory (ESO) under programs 0113.D-0255(A) (GJ 783 A; PI: Campante) and 0113.D-0255(B) (GJ 570 A; PI: Campante). This work was supported by Fundação para a Ciência e a Tecnologia (FCT) through research grant UID/04434/2025. This work was supported by national funds through FCT under project 2024.15303.PEX. TLC is supported by FCT in the form of a work contract (2023.08117.CEECIND/CP2839/CT0004). YZ acknowledges support from the European Union's Horizon 2020 research and innovation program under Marie Skłodowska-Curie grant agreement no. 101150921. TRB is supported by the Australian Research Council through Laureate Fellowship FL220100117. EC acknowledges support from the research grant "Unveiling the magnetic side of the Stars" (PI: A. Bonanno) funded under the INAF national call for Fundamental Research 2023. MSC is supported by FCT in the form of a work contract (2023.09303.CEECIND/CP2839/CT0003). This work was funded by the European Union (ERC, FIERCE, 101052347). Views and opinions expressed are, however, those of the authors only and do not necessarily reflect those of the European Union or the European Research Council. Neither the European Union nor the granting authority can be held responsible for them. The authors thank Anish Amarsi and Thomas Nordlander for valuable comments and fruitful discussions.

References

Adibekyan, V., Figueira, P., Santos, N. C., et al. 2015, A&A, 583, A94
Adibekyan, V., Sousa, S. G., Santos, N. C., et al. 2012, A&A, 545, A32
Aerts, C. 2021, Reviews of Modern Physics, 93, 015001
Allen, C., Poveda, A., & Herrera, M. A. 2000, A&A, 356, 529
Angulo, C. 1999, in American Institute of Physics Conference Series, Vol. 495, Experimental Nuclear Physics in Europe: Facing the next millennium (AIP), 365
Arentoft, T., Kjeldsen, H., Bedding, T. R., et al. 2008, ApJ, 687, 1180
Asplund, M., Grevesse, N., Sauval, A. J., & Scott, P. 2009, ARA&A, 47, 481
Baglin, A., Auvergne, M., Barge, P., et al. 2006, in ESA Special Publication, Vol. 1306, The CoRoT Mission Pre-Launch Status - Stellar Seismology and Planet Finding, ed. M. Fridlund, A. Baglin, J. Lochard, & L. Conroy, 33
Bailer-Jones, C. A. L., Rybizki, J., Fouesneau, M., Demleitner, M., & Andrae, R. 2021, AJ, 161, 147
Ball, W. H. & Gizon, L. 2014, A&A, 568, A123
Baudin, F., Samadi, R., Goupil, M.-J., et al. 2005, A&A, 433, 349
Bazot, M., Ireland, M. J., Huber, D., et al. 2011, A&A, 526, L4
Bedding, T. R., Kjeldsen, H., Butler, R. P., et al. 2004, ApJ, 614, 380
Bonanno, A., Corsaro, E., Del Sordo, F., et al. 2019, A&A, 628, A106
Bonanno, A., Corsaro, E., & Karoff, C. 2014, A&A, 571, A35
Boro Saikia, S., Marvin, C. J., Jeffers, S. V., et al. 2018, A&A, 616, A108
Borucki, W. J., Koch, D., Basri, G., et al. 2010, Science, 327, 977
Boyajian, T. S., von Braun, K., van Belle, G., et al. 2012, ApJ, 757, 112
Brown, T. M., Gilliland, R. L., Noyes, R. W., & Ramsey, L. W. 1991, ApJ, 368, 599
Burgasser, A. J., Kirkpatrick, J. D., Cutri, R. M., et al. 2000, ApJ, 531, L57
Burt, J. A., Dumusque, X., & Halverson, S. 2025, arXiv e-prints, arXiv:2511.01954
Campante, T. L., Barclay, T., Swift, J. J., et al. 2015, ApJ, 799, 170
Campante, T. L., Chaplin, W. J., Lund, M. N., et al. 2014, ApJ, 783, 123
Campante, T. L., Kjeldsen, H., Li, Y., et al. 2024, A&A, 683, L16
Campante, T. L., Schofield, M., Kuszlewicz, J. S., et al. 2016, ApJ, 830, 138
Carrier, F. & Eggenberger, P. 2006, A&A, 450, 695
Chaplin, W. J., Bedding, T. R., Bonanno, A., et al. 2011, ApJ, 732, L5
Chaplin, W. J., Elsworth, Y., Houdek, G., & New, R. 2007, MNRAS, 377, 17
Chaplin, W. J., Elsworth, Y., Isaak, G. R., Miller, B. A., & New, R. 2000, MNRAS, 313, 32
Chaplin, W. J. & Miglio, A. 2013, ARA&A, 51, 353
Christensen-Dalsgaard, J. & Frandsen, S. 1983, Sol. Phys., 82, 469
Christensen-Dalsgaard, J. & Gough, D. O. 1982, MNRAS, 198, 141
Collet, R., Nordlund, Å., Asplund, M., Hayek, W., & Trampedach, R. 2018, MNRAS, 475, 3369
Crawford, C. L., Li, Y., Huber, D., et al. 2025, MNRAS, 542, 3289
Cyburt, R. H., Amthor, A. M., Ferguson, R., et al. 2010, ApJS, 189, 240
Dall, T. H., Bruntt, H., Stello, D., & Strassmeier, K. G. 2010, A&A, 514, A25
Davies, G. R., Handberg, R., Miglio, A., et al. 2014, MNRAS, 445, L94

Dekker, H., D'Odorico, S., Kaufer, A., Delabre, B., & Kotzlowski, H. 2000, in Society of Photo-Optical Instrumentation Engineers (SPIE) Conference Series, Vol. 4008, Optical and IR Telescope Instrumentation and Detectors, ed. M. Iye & A. F. Moorwood, 534
Duncan, D. K., Vaughan, A. H., Wilson, O. C., et al. 1991, ApJS, 76, 383
Eddington, A. S. 1926, The Internal Constitution of the Stars (Cambridge University Press)
ESA, ed. 1997, ESA Special Publication, Vol. 1200, The HIPPARCOS and TYCHO catalogues. Astrometric and photometric star catalogues derived from the ESA HIPPARCOS Space Astrometry Mission
Feiden, G. A. & Chaboyer, B. 2012, ApJ, 757, 42
Ferguson, J. W., Alexander, D. R., Allard, F., et al. 2005, ApJ, 623, 585
Frandsen, S., Jones, A., Kjeldsen, H., et al. 1995, A&A, 301, 123
Fröhlich, C., Romero, J., Roth, H., et al. 1995, Sol. Phys., 162, 101
Gaia Collaboration, Vallenari, A., Brown, A. G. A., et al. 2023, A&A, 674, A1
García, R. A., Mathur, S., Salabert, D., et al. 2010, Science, 329, 1032
Geballe, T. R., Saumon, D., Leggett, S. K., et al. 2001, ApJ, 556, 373
Gibson, S. R., Howard, A. W., Rider, K., et al. 2024, in Society of Photo-Optical Instrumentation Engineers (SPIE) Conference Series, Vol. 13096, Ground-based and Airborne Instrumentation for Astronomy X, ed. J. J. Bryant, K. Motohara, & J. R. D. Vernet, 1309609
Gold, R. 1964, An iterative unfolding method for response matrices, Vol. 6984 (Argonne National Laboratory)
Gomes da Silva, J., Figueira, P., Santos, N. C., & Faria, J. 2018, The Journal of Open Source Software, 3, 667
Gomes da Silva, J., Santos, N. C., Adibekyan, V., et al. 2021, A&A, 646, A77
Goupil, M.-J., Catala, C., Samadi, R., et al. 2024, A&A, 683, A78
Gray, R. O., Corbally, C. J., Garrison, R. F., et al. 2006, AJ, 132, 161
Grundahl, F., Kjeldsen, H., Christensen-Dalsgaard, J., Arentoft, T., & Frandsen, S. 2007, Communications in Asteroseismology, 150, 300
Harvey, J. W. 1988, in Advances in Helio- and Asteroseismology, ed. J. Christensen-Dalsgaard & S. Frandsen, Vol. 123, 497
Hatt, E., Nielsen, M. B., Chaplin, W. J., et al. 2023, A&A, 669, A67
Henry, T. J., Soderblom, D. R., Donahue, R. A., & Baliunas, S. L. 1996, AJ, 111, 439
Hon, M., Huber, D., Li, Y., et al. 2024, ApJ, 975, 147
Houdek, G. 2006, in ESA Special Publication, Vol. 624, Proceedings of SOHO 18/GONG 2006/HELAS I, Beyond the spherical Sun, ed. K. Fletcher & M. Thompson, 28
Houdek, G., Balmforth, N. J., Christensen-Dalsgaard, J., & Gough, D. O. 1999, A&A, 351, 582
Houdek, G. & Dupret, M.-A. 2015, Living Reviews in Solar Physics, 12, 8
Hourihane, A., François, P., Worley, C. C., et al. 2023, A&A, 676, A129
Howell, S. B., Sobeck, C., Haas, M., et al. 2014, PASP, 126, 398
Iglesias, C. A. & Rogers, F. J. 1996, ApJ, 464, 943
Isaak, G. R., McLeod, C. P., Pallé, P. L., van der Raay, H. B., & Roca Cortés, T. 1989, A&A, 208, 297
Jacoutot, L., Kosovichev, A. G., Wray, A., & Mansour, N. N. 2008, ApJ, 684, L51
Jenkins, J. S., Murgas, F., Rojo, P., et al. 2011, A&A, 531, A8
Kitiashvili, I. N., Kosovichev, A. G., Mansour, N. N., & Wray, A. A. 2011, Sol. Phys., 268, 283
Kjeldsen, H. & Bedding, T. R. 1995, A&A, 293, 87
Kjeldsen, H. & Bedding, T. R. 2011, A&A, 529, L8
Kjeldsen, H. & Bedding, T. R. 2012, in IAU Symposium, Vol. 285, New Horizons in Time Domain Astronomy, ed. E. Griffin, R. Hanisch, & R. Seaman, 17
Kjeldsen, H., Bedding, T. R., Arentoft, T., et al. 2008a, ApJ, 682, 1370
Kjeldsen, H., Bedding, T. R., Butler, R. P., et al. 2005, ApJ, 635, 1281
Kjeldsen, H., Bedding, T. R., & Christensen-Dalsgaard, J. 2008b, ApJ, 683, L175
Kjeldsen, H., Bedding, T. R., Li, Y., et al. 2025, A&A, 700, A39
Kuhfuss, R. 1986, A&A, 160, 116
Kurucz, R. L. 1993, SYNTHE spectrum synthesis programs and line data (Astrophysics Source Code Library)
Li, Y., Huber, D., Ong, J. M. J., et al. 2025a, ApJ, 984, 125
Li, Y., Liu, M. C., Dupuy, T. J., et al. 2025b, arXiv e-prints, arXiv:2512.06083
Liu, M. C., Leggett, S. K., & Chiu, K. 2007, ApJ, 660, 1507
Lomb, N. R. 1976, Ap&SS, 39, 447
Luhn, J. K., Robertson, P., Halverson, S., et al. 2025, ApJ, 987, 168
Lund, M. N., Chontos, A., Grundahl, F., et al. 2025, A&A, 701, A285
Lund, M. N., Silva Aguirre, V., Davies, G. R., et al. 2017, ApJ, 835, 172
Lundkvist, M. S., Kjeldsen, H., Albrecht, S., et al. 2016, Nature Communications, 7, 11201
Lundkvist, M. S., Kjeldsen, H., Bedding, T. R., et al. 2024, ApJ, 964, 110
Magic, Z., Collet, R., Asplund, M., et al. 2013, A&A, 557, A26
Mamajek, E. E. & Hillenbrand, L. A. 2008, ApJ, 687, 1264
Mamajek, E. E. & Stapelfeldt, K. 2024, arXiv e-prints, arXiv:2402.12414
Mathur, S., Huber, D., Batalha, N. M., et al. 2017, ApJS, 229, 30
Mayor, M., Pepe, F., Queloz, D., et al. 2003, The Messenger, 114, 20
Moedas, N., Deal, M., Bossini, D., & Campilho, B. 2022, A&A, 666, A43
Morháč, M., Matoušek, V., & Kliman, J. 2003, Digital Signal Processing, 13, 144
Nordlund, Å. & Galsgaard, K. 1995, Tech. rep., Astronomical Observatory, Copenhagen University
Nordlund, Å. & Stein, R. F. 2001, ApJ, 546, 576
Paxton, B., Smolec, R., Schwab, J., et al. 2019, ApJS, 243, 10
Pepe, F., Cristiani, S., Rebolo, R., et al. 2021, A&A, 645, A96
Phillips, M. W., Tremblin, P., Baraffe, I., et al. 2020, A&A, 637, A38
Rains, A. D., Ireland, M. J., White, T. R., Casagrande, L., & Karovicova, I. 2020, MNRAS, 493, 2377
Rauer, H., Aerts, C., Cabrera, J., et al. 2025, Experimental Astronomy, 59, 26
Rendle, B. M., Buldgen, G., Miglio, A., et al. 2019, MNRAS, 484, 771
Ricker, G. R., Winn, J. N., Vanderspek, R., et al. 2015, Journal of Astronomical Telescopes, Instruments, and Systems, 1, 014003
Salaris, M., Chieffi, A., & Straniero, O. 1993, ApJ, 414, 580
Samadi, R., Georgobiani, D., Trampedach, R., et al. 2007, A&A, 463, 297
Samadi, R., Goupil, M.-J., Alecian, E., et al. 2005, Journal of Astrophysics and Astronomy, 26, 171
Samadi, R., Ludwig, H.-G., Belkacem, K., et al. 2010a, A&A, 509, A16
Samadi, R., Ludwig, H.-G., Belkacem, K., Goupil, M.-J., & Dupret, M.-A. 2010b, A&A, 509, A15
Samus, N. N., Kazarovets, E. V., Durlevich, O. V., Kireeva, N. N., & Pastukhova, E. N. 2017, Astronomy Reports, 61, 80
Santos, N. C., Sousa, S. G., Mortier, A., et al. 2013, A&A, 556, A150
Saumon, D., Marley, M. S., Cushing, M. C., et al. 2006, ApJ, 647, 552
Sayeed, M., Huber, D., Chontos, A., & Li, Y. 2025, AJ, 170, 212
Scargle, J. D. 1982, ApJ, 263, 835
Sneden, C. A. 1973, PhD thesis, The University of Texas at Austin
Sonoi, T., Samadi, R., Belkacem, K., et al. 2015, A&A, 583, A112
Soubiran, C., Brouillet, N., & Casamiquela, L. 2022, A&A, 663, A4
Sousa, S. G. 2014, in Determination of Atmospheric Parameters of B-, A-, F- and G-Type Stars, ed. E. Niemczura, B. Smalley, & W. Pych, 297
Sousa, S. G., Adibekyan, V., Delgado-Mena, E., et al. 2021, A&A, 656, A53
Sousa, S. G., Santos, N. C., Adibekyan, V., Delgado-Mena, E., & Israelian, G. 2015, A&A, 577, A67
Sousa, S. G., Santos, N. C., Israelian, G., Mayor, M., & Monteiro, M. J. P. F. G. 2007, A&A, 469, 783
Stassun, K. G., Oelkers, R. J., Paegert, M., et al. 2019, AJ, 158, 138
Stein, R. F. & Nordlund, Å. 2001, ApJ, 546, 585
Stein, R. F., Nordlund, Å., Collet, R., & Trampedach, R. 2024, ApJ, 970, 24
Tassoul, M. 1980, ApJS, 43, 469
Teixeira, T. C., Kjeldsen, H., Bedding, T. R., et al. 2009, A&A, 494, 237
Thoul, A. A., Bahcall, J. N., & Loeb, A. 1994, ApJ, 421, 828
Toutain, T. & Appourchaux, T. 1994, A&A, 289, 649
Townsend, R. H. D. & Teitler, S. A. 2013, MNRAS, 435, 3406
Tsantaki, M., Sousa, S. G., Adibekyan, V., et al. 2013, A&A, 555, A150
Vaughan, A. H. & Preston, G. W. 1980, PASP, 92, 385
Verner, G. A., Elsworth, Y., Chaplin, W. J., et al. 2011, MNRAS, 415, 3539
White, T. R., Bedding, T. R., Stello, D., et al. 2011a, ApJ, 742, L3
White, T. R., Bedding, T. R., Stello, D., et al. 2011b, ApJ, 743, 161
Woodard, M. F. 1984, PhD thesis, University of California, San Diego
Zechmeister, M. & Kürster, M. 2009, A&A, 496, 577
Zhou, Y., Asplund, M., & Collet, R. 2019, ApJ, 880, 13
Zhou, Y., Asplund, M., Collet, R., & Joyce, M. 2020, MNRAS, 495, 4904

List of Objects